

ADEPT: A Noninvasive Method for Determining Elastic Properties of Valve Tissue

Wensi Wu^{1,2}, Mitchell Daneker^{3,4}, Christian Herz¹, Hannah Dewey¹, Jeffrey A. Weiss⁵, Alison M. Pouch^{6,7}, Lu Lu^{3,*}, and Matthew A. Jolley^{1,2,*}

¹Department of Anesthesiology and Critical Care Medicine, Children's Hospital of Philadelphia, Philadelphia, PA, USA

²Division of Cardiology, Children's Hospital of Philadelphia, Philadelphia, PA, USA

³Department of Statistics and Data Science, Yale University, New Haven, CT, USA

⁴Department of Chemical and Biochemical Engineering, University of Pennsylvania, Philadelphia, PA, USA

⁵Department of Biomedical Engineering, Scientific Computing and Imaging Institute, University of Utah, Salt Lake City, UT, USA

⁶Department of Bioengineering, University of Pennsylvania, Philadelphia, PA, USA

⁷Department of Radiology, University of Pennsylvania, Philadelphia, PA, USA

*Corresponding authors. Email: lu.lu@yale.edu, jolleym@chop.edu

ABSTRACT

Valvular heart disease accounts for up to 20% of cardiac surgery in the United States. Computer simulation of “virtual interventions” may inform optimal valve repair for a given patient prior to intervention. However, there is a paucity of methods to noninvasively determine *in vivo* mechanical properties of valve tissue from clinically acquired 3D images, limiting the accuracy of computer prediction and translational potential of *in silico* valve repairs. Here, we propose ADEPT, **A** noninvasive method for **D**etermining **E**lastic **P**roperties of valve **T**issue, to overcome this methodological gap. Our framework combines image registration and physics-informed neural networks (PINNs) to estimate material properties of valve tissue from 3D echocardiograms (3DE). The PINN model was validated on a series of benchmarks before being applied to the 3DE of the tricuspid valve in a child with congenital heart disease. Our approach yielded accurate material parameter estimations in the examples accompanying this work.

1 Introduction

Valvular heart disease is a leading contributor to cardiovascular morbidity and mortality, affecting nearly 41 million people worldwide^{1,2}, and accounts for about 20% of cardiac surgery in the United States. Valve dysfunction can manifest as stenosis (*i.e.*, valves cannot fully open, restricting blood flow) or regurgitation (*i.e.*, valves cannot adequately coapt, allowing backward flow). Both heart valve stenosis and regurgitation lead to decreased efficiency of circulation, resulting in heart failure, end-organ (*e.g.*, lung, kidney) dysfunction, or death^{3,4}. In this context, valve repair, either surgical or transcatheter, is increasingly applied to restore valvular function^{5,6}. While 3D imaging, including 3D echocardiography (3DE), has greatly informed valve assessment and repair by providing an intuitive view of the functioning valve directly to the surgeon, 3D visualization alone is insufficient for quantitative analysis of the valve^{7–11}. Image-based valve modeling has partially unlocked this capability, allowing for precise, quantitative geometric comparison of normal valves to dysfunctional valves. This, in turn, has improved the understanding of the relationship between 3D valve structure and valve dysfunction in both adults^{7,8,12,13} and children^{14–18}.

However, understanding associations of valve structure to valve function cannot infer causation. Although conventional image-based valve structural modeling offers critical insights into the structural

features of diseased valves by analyzing variations in valve morphology across a population, insights gained are statistical generalizations typically based on a singular, static systolic frame. Further, geometry-based modeling does not capture the kinematic trajectory or the underlying mechanics of heart valves, and cannot be used as predictive tools to realistically model dynamic valve function or repair. As such, determining which valves can be repaired and how to best repair an individual dysfunctional valve remains a significant challenge^{19,20}.

The application of physics-based computational models (*e.g.*, finite element analysis) has begun to provide this capability, enabling the potential to determine patient-specific structural contributors to valve failure (*e.g.*, stress, strain)^{21,22}, as well as the long-term possibility for the iterative optimization of valve repair in an individual patient^{23–28}. Such modeling is particularly relevant in congenital heart disease where procedural optimization is unlikely to occur via human randomized clinical trials given the number of potential methods for repair, heterogeneity of anatomy, duration to complete such studies, and reticence to vary from established techniques in a vulnerable population²⁷. While particularly relevant to children, these tenets remain relevant to all populations at risk of valve dysfunction. Toward that end, image-derived computational approaches directed toward understanding risk factors for valve failure and repair optimization have the potential to reduce the need for a trial-and-error approach, and allow identification of the ideal repair for an individual patient before intervention (image-derived precision medicine).

However, truly patient specific models of valve closure and repair will depend on not just the knowledge of the valve structure, but also the mechanical properties of the individual leaflet that relate a given load to the resulting leaflet deformation²⁹. Tissue mechanical properties are typically characterized by calibrating the material constants of a pre-defined material constitutive description within a forward numerical model, until the simulated strain fields match with empirical observations. Traditional material characterization entails two steps: 1) accurately measure the physical strain fields to provide a reference in the calibration process, and 2) iteratively solve the inverse problem to determine the parameters in the constitutive model until the simulated strain fields match with the reference ones. Several approaches to estimate reference leaflet strain fields have been proposed: *ex vivo* biaxial test³⁰, *in vivo* marker tracking³¹, and 3D leaflet reconstruction and spline fitting³². Unfortunately, these approaches either alter the native environment of tissues, require invasive procedures, or specialize in specific valve types. For these reasons, they are fundamentally limited in their practical application to modeling of human disease.

Ideally, patient-specific material properties could be obtained from an individual patient's 3D images and utilized along with valve structure in personalized simulations of valve function and repair^{29,33}. Such a noninvasive approach to quantify patient-specific tissue mechanical properties (*e.g.*, Young's modulus and Poisson's ratio) is critical to accurately simulate *in vivo* heart valve dynamics and allow for iterative testing and systematic comparison of repair strategies in an individual patient. To meet this need, we propose a general and noninvasive framework, combining deformable image registration^{34,35} and physics-informed neural networks (PINNs)^{36–38}, to obtain accurate patient-specific tissue elastic properties from clinically acquired 4D (3D + time) images. PINNs are deep learning-based partial differential equation (PDE) solvers that are particularly powerful for identifying unknown parameters in inverse studies^{39–46}. It has the advantage of simultaneously analyzing *in vivo* leaflets mechanics and determining their constitutive properties to ensure the solution satisfies both empirical observations and the governing principles.

The present work serves as the point of departure for a noninvasive approach to identify *in vivo* tissue properties that are more applicable to human studies. Specifically, this advancement enables the identification of tissue elastic properties unique to each individual, signifies a critical step towards the development of digital twins of heart valves, and unleashes the latent potential of high-fidelity computational models of virtual surgical intervention. The proposed approach is fundamentally applicable

to multi-modal 4D images (*e.g.*, 3DE, computed tomography, magnetic resonance imaging) of any heart valve. In this proof-of-concept study, 3DE images of a regurgitant tricuspid valve of an 11-year-old patient with hypoplastic left heart syndrome (single ventricle congenital heart disease) were chosen as the initial application.

This paper is organized as follows. In Section 2, we provide an overview of ADEPT and present the problem descriptions and parameter validation results for each example. In Sections 3 and 4, we discuss the clinical implications, major contributions, limitations and future direction of the current work. In Section 5, we provide theoretical background and formulation of image registration, PINNs, and material constitutive models concerning this work.

2 Results

We considered four examples in this work: a 2D thick-walled cylinder subjected to internal pressure, a 2D thin circular plate subjected to transverse pressure, a 3D truncated cone subjected to external pressure, and a 3DE-derived tricuspid valve subjected to transvalvular pressure. In each example, we trained a PINN model to determine the “unknown” elastic properties from reference displacement data. To verify solution accuracy and improve the interpretability of PINN-prediction, we computed the mechanical responses resulting from the estimated material parameters using the analytical formulation (if it exists) or first-principle solvers (*e.g.*, FEBio finite element package⁴⁷). The mechanical responses were subsequently compared to the reference solution to evaluate their agreement. All PINN experiments were trained on a NVIDIA H100 80GB GPU.

2.1 Overview of material parameter identification procedure

An overview of the proposed method is presented in Fig. 1. Fig. 1A illustrates the geometry of the examples considered in the work; relevant problem formulation and descriptions specific to each example are provided in Sections 2.2 to 2.5. Fig. 1B presents the general workflow of our prediction-validation procedure. In examples 1, 3, and 4, a parallel neural network architecture with two independent feedforward neural networks (FNNs) was chosen for the PINN model, given its efficiency and effectiveness, as demonstrated in our previous work⁴⁴. The Cartesian coordinates (x , y , and z) of the object were the input for the FNNs, with one network outputting displacements and the other outputting stresses. We subsequently constructed a loss function by setting up penalty terms on momentum equilibrium, material constitutive balance, and kinematics constraints (*i.e.*, enforcing displacement agreement between predicted values and reference data). At each iteration, the network weights and biases (denoted as θ_{NN}) and the unknown material parameters (denoted as θ_{MAT}) were iteratively optimized until the loss function was minimized. In example 2, only the displacement network was needed to inform prediction. As such, the material constitutive balance was ignored in this example.

We computed the reference displacements of the first and second examples from analytical formulations. Displacements from the third example were computed using finite element analysis (FEA), whereas those of patient-specific tricuspid valves were estimated using an image registration approach, described in Fig. 1D. In particular, 3D TEE image volumes of two consecutive frames were registered using a non-symmetric diffeomorphic image registration algorithm³⁴. This step resulted in a voxel-wise transformation matrix, ϕ , that maps the image intensity from the moving to the fixed 3D TEE image volume. The transformation matrix, ϕ , was subsequently applied to a manual segmentation of the open leaflets in order to estimate the closed leaflet geometry. The differences between the nodal points of the open and closed valves were calculated, serving as reference displacement fields.

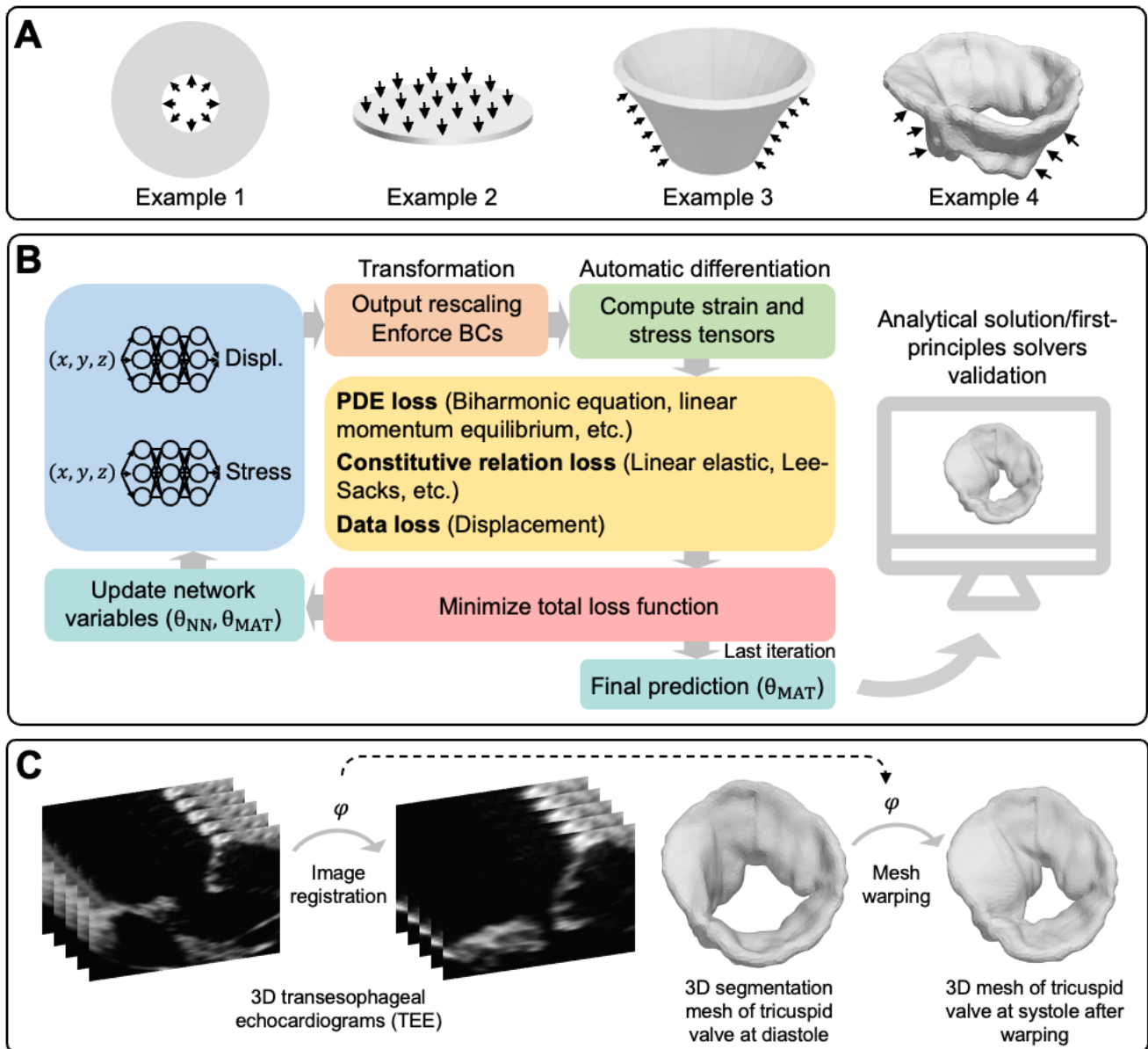


Figure 1. Material parameter identification procedure. (A) Example cases considered in the current study were a 2D thick-walled cylinder subject to internal pressure (example 1), a 2D thin circular plate subjected to transverse pressure (example 2), a 3D truncated cone subject to external pressure (example 3), and a 3D image-derived patient-specific regurgitant tricuspid valve model subject to transvalvular pressure (example 4). (B) The PINN architecture contained a two-layer parallel network with two feedforward networks that independently predict displacements and stresses. The reference displacement data of the example cases were used to guide the minimization of data loss in PINNs. In examples 1 and 2, the analytical solutions of displacements were sought. Displacements in example 3 were estimated through FEA, and those in example 4 were approximated using deformable image registration illustrated in (C).

2.2 2D thick-walled cylinder subjected to internal pressure

2.2.1 Problem description

We started with a 2D linear elastic example, as illustrated in Fig. 2A, to verify the efficacy of our proposed methods. The strong-form static momentum equation, $\sigma_{ij,j} = 0$, was the governing PDE, where σ_{ij} represents the Cauchy-stress. A thick-walled cylinder with an inner radius of $1 \mu\text{m}$ and an outer radius of $5 \mu\text{m}$ was subjected to $10^{-5} \text{ N}/\mu\text{m}^2$ uniform internal pressure. The ground truth solution of the thick-walled

cylinder was calculated with Young's modulus and Poisson's ratio of $0.135 \text{ N}/\mu\text{m}^2$ and 0.3 , respectively. Here, we reduced our analysis to one-quarter of the cylinder due to symmetry in geometry and pressure load. An isotropic linear elastic material model was assumed.

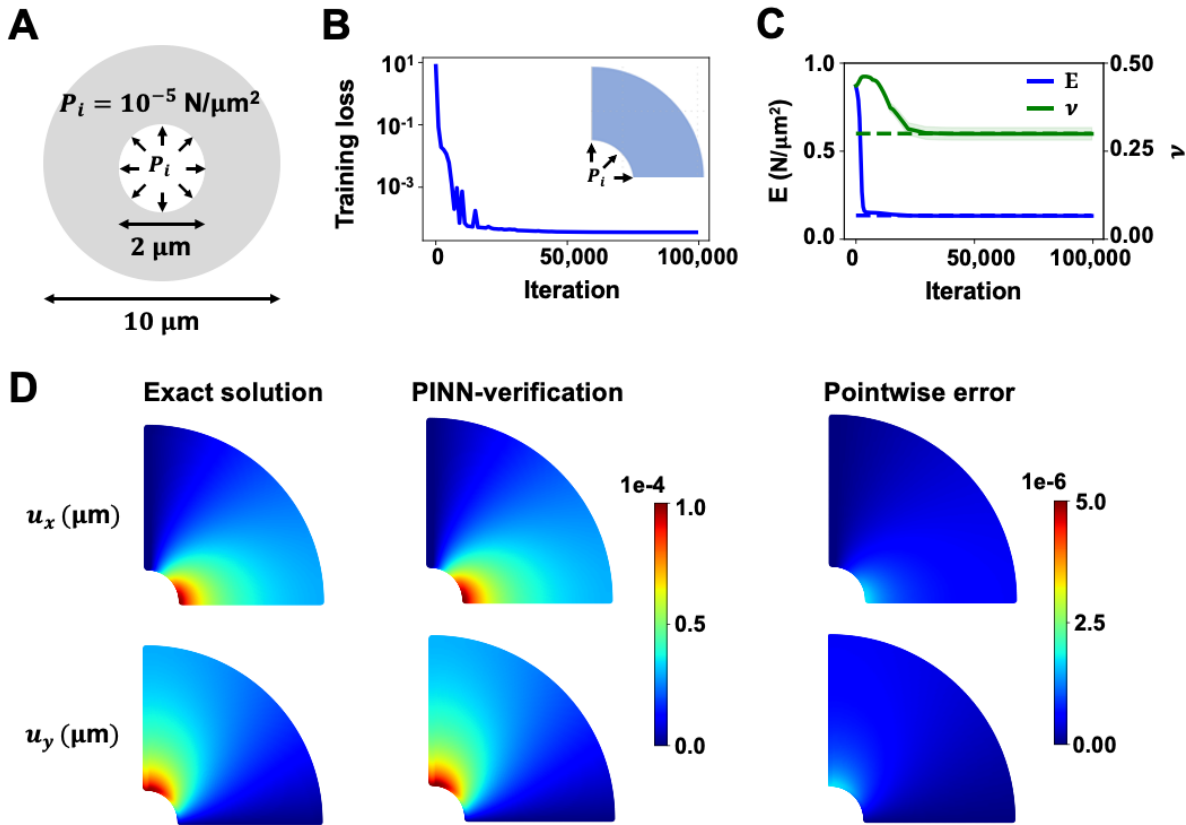


Figure 2. 2D thick-walled cylinder verification results. (A) A hollow cylinder with $1 \mu\text{m}$ inner radius and $5 \mu\text{m}$ outer radius is shown. A uniform pressure load of $10^{-5} \text{ N}/\mu\text{m}^2$ is applied to the wall of the inner radius of the cylinder. (B) The training loss history is shown. The total training loss converges to below 10^{-3} at 100,000 iterations. (C) The average and standard deviation of E and ν estimated from 10 repeated PINN analyses (solid lines) are plotted along with the ground truth values (dotted lines). The relative errors of E and ν were 1.72% and 0.23% , respectively. (D) The exact solution, PINN-verification, and pointwise errors of displacement are presented. The estimated E and ν produced highly accurate displacement fields with pointwise errors in $\mathcal{O}(10^{-6})$.

2.2.2 Estimated results from PINNs

We adopted a parallel architecture with two independent neural networks. Each independent network within PINN was assigned 5 hidden layers with 45 neurons per layer. The loss weights were $w_{\text{PDEs}} = 1$, $w_{\text{M}} = 10$, and $w_{\text{D}} = 1$. The subscript M refers to material model and D refers to displacement reference data. The learning rate decay was set to 10^{-3} with a decay rate of 0.15 every $15,000$ iterations. The neural networks were trained using the Adam optimizer for $100,000$ iterations. The total training loss, which includes losses in the PDEs, stress-strain relations, reference data observation, and traction condition, converged to a satisfactory value of below 10^{-3} at the end of the analysis, as demonstrated in Fig. 2B. The PINN inverse analysis was repeated 10 times with varying random seeds to evaluate its robustness and precision in different network weight initialization. A total of $1,500$ PDE and $1,500$ data collocation points were used in the training. The average runtime of the 10 repeated tests was 0.5 hours.

The prediction histories of the mean and standard deviation of Young's modulus (E) and Poisson's ratio (ν) are presented in Fig. 2C. The dotted lines denote the ground truth values, while the solid lines denote PINN estimation. Similar to our previous work^{42,44}, we constrained the search range of E and ν to a reasonable range of $[0, 1]$ N/ μm^2 and $[0, 0.5]$, respectively, to facilitate the optimization effort. The mean and standard deviation values of E and ν of the 10 repeated tests were 0.133 ± 0.002 N/ μm^2 and 0.299 ± 0.018 , respectively. The relative error of the average E was 1.72%, and the average ν was 0.23%.

2.2.3 Validation against analytical solution

Fig. 2D provides the displacement and stress responses between the ground truth and the verification results with PINN-estimated E and ν . The analytical solutions for displacements in Cartesian coordinates were calculated from the following forms:

$$u_x(x, y) = \frac{r_i^2 P_i r}{E(r_o^2 - r_i^2)} \left[1 - \nu + \left(\frac{r_o}{r}\right)^2 (1 + \nu) \right] \cos(\theta),$$

and

$$u_y(x, y) = \frac{r_i^2 P_i r}{E(r_o^2 - r_i^2)} \left[1 - \nu + \left(\frac{r_o}{r}\right)^2 (1 + \nu) \right] \sin(\theta).$$

In this paper, r_i and r_o are the inner and outer radius. r and θ are the equivalent radius and angle in polar coordinate, defined as $r = \sqrt{x^2 + y^2}$ and $\theta = \arctan(y/x)$. P_i is the internal pressure. The estimated displacements using material parameters derived from PINNs were in excellent agreement with the analytical solution. The maximum pointwise errors of displacements were $\mathcal{O}(10^{-6})$, and the L^2 relative errors of u_x and u_y were both within 1.71%.

2.3 Deflected circular plate subjected to uniform pressure

2.3.1 Problem description

The second benchmark considered in this work was a thin circular plate with 1 MN/ m^2 uniform pressure applied to its top surface, illustrated in Fig. 3A. The biharmonic equation, $\nabla^2 \nabla^2 u_z = \frac{q}{D}$ was taken as the governing PDEs of this system. Herein, u_z is the out-of-plane displacement, q is the uniform applied pressure, σ_{ij} is the Cauchy-stress, and D is the plate flexural rigidity. Further, D is given by $D = \frac{H^3 E}{12(1-\nu^2)}$ with H denotes plate thickness. The circular plate has a radius of 1 m and a thickness of 0.1 m. It was subjected to a clamped boundary condition along its edge, and an isotropic linear elastic material model was assumed. The ground truth out-of-plane displacements of the circular plate were determined using E and ν of 1 MN/ m^2 and 0.3, respectively.

2.3.2 Estimated results from PINNs

In this example, given the direct relation between the out-of-plane displacements and the elastic parameters in the biharmonic equation, only a displacement network was needed to facilitate the parameter prediction. As such, we only considered the PDE loss in the biharmonic equation and data loss. The loss weights were $w_{\text{PDEs}} = 1$, and $w_d = 10^3$. The learning rate decay was set to 10^{-3} with a decay rate of 0.15 every 15,000 iterations. The neural networks were trained using the Adam optimizer for 100,000 iterations. The total training loss converged to a satisfactory value of below 10^{-4} at the end of the analysis, as demonstrated in Fig. 3B. A total of 5,000 PDE and 5,000 data collocation points were used in the training. The average runtime for this benchmark was 2.8 hours.

The prediction histories of the mean and standard deviation of E and ν are presented in Fig. 3C. We defined a reasonable search range of $[0, 2]$ N/ μm^2 and $[0, 0.5]$ for E and ν , respectively. The mean and standard deviation values of E and ν of the 10 repeated tests were 1.003 ± 0.002 N/ μm^2 and 0.296 ± 0.002 , respectively. The relative error of E_{avg} was 0.311%, and ν_{avg} was 1.489%.

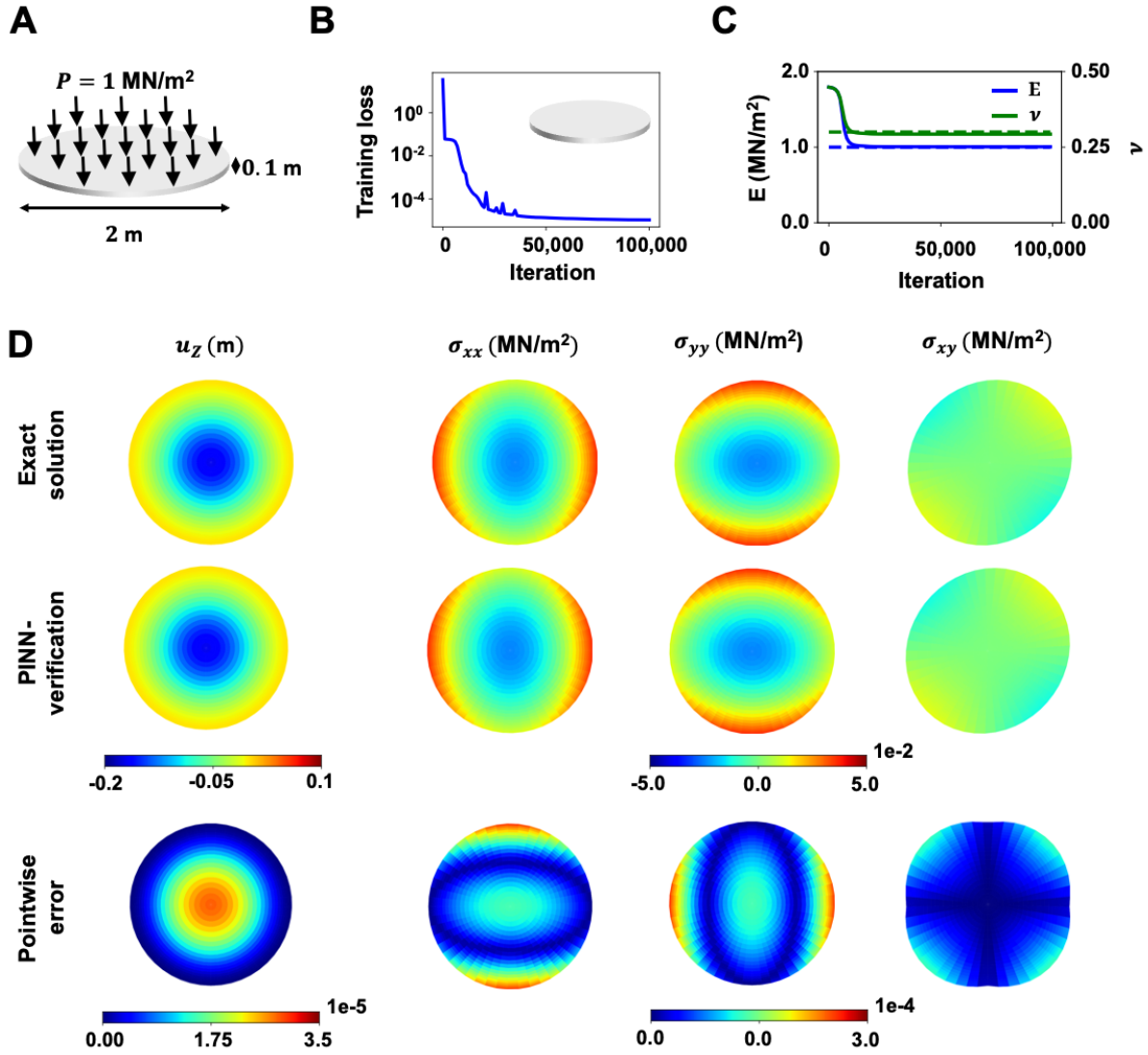


Figure 3. Deflected circular plate verification results. (A) A thin circular plate with 1 m radius and 0.1 m thickness is shown. A uniform pressure load of 1MN/m^2 is applied to its top surface. (B) The training loss history is shown. The total training loss converges to below 10^{-4} at the end of analysis. (C) The average and standard deviation of E and ν estimated from 10 repeated PINN analyses (solid lines) are plotted along with the ground truth values (dotted lines). The relative errors of E_{avg} and ν_{avg} were 0.312% and 1.489%, respectively. (D) The exact solution, PINN-verification, and pointwise errors of displacement and stress are presented. The absolute pointwise error of the out-of-plane displacements and in-plane stresses are in $\mathcal{O}(10^{-5})$ and $\mathcal{O}(10^{-4})$, respectively.

2.3.3 Validation against analytical solution

Fig. 3D provides the out-of-plane displacement and the in-plane stress responses on the top surface of the plate (stresses of the mid-surface are zero based on the Kirchhoff-Love plate theory) between the ground truth and the verification results. The out-of-plane displacements were calculated from the following analytical forms:

$$u_z(x, y) = \frac{q}{64D} [a^2 - (x^2 + y^2)]^2,$$

where a is the radius of the plate. The analytical solutions of in-plane stresses on the top surface are given by:

$$\begin{aligned}\sigma_{xx}(x, y, z) &= \frac{-Ez}{1-\nu^2} \left(\frac{\delta^2 u_z}{\delta x^2} + \nu \frac{\delta^2 u_z}{\delta y^2} \right), \\ \sigma_{yy}(x, y, z) &= \frac{-Ez}{1-\nu^2} \left(\frac{\delta^2 u_z}{\delta y^2} + \nu \frac{\delta^2 u_z}{\delta x^2} \right), \\ \text{and } \sigma_{xy}(x, y, z) &= \frac{-Ez}{1+\nu} \frac{\delta^2 u_z}{\delta x \delta y},\end{aligned}$$

with $z = 0.05$, half the plate thickness. The L^2 relative error of u_z was 0.019%. The L^2 relative errors of σ_{xx} , σ_{yy} , σ_{xy} were 0.378%, 0.387%, and 0.638%, respectively.

2.4 3D truncated cone subjected to external pressure

2.4.1 Problem description

As a step towards a more realistic representation of the tricuspid valve geometry, we modified our PINN model to estimate the material parameters of a hollow 3D truncated cone, displayed in Fig. 4A. Similarly, the strong-form static momentum equation, $\sigma_{ij,j} = 0$, was selected as the governing PDE due to quasi-static loading and small deformation nature of this example. The 3D truncated cone was 1 mm tall with a 0.1 mm thick outer surface. The diameters of the top and bottom ends were 2 mm and 1 mm, respectively. The ground truth solution was generated with Young's modulus and Poisson's ratio of 5 N/mm² and 0.3, respectively. Pinned boundary conditions ($u_x=u_y=u_z=0$) were prescribed to the top edge of the cone. A uniform external pressure of 0.01 N/mm² was applied to the external surface of the cone. An isotropic linear elastic material model was assumed.

2.4.2 Estimated results from PINNs

A parallel architecture with two independent neural networks was adopted. Each independent network in PINN was assigned 5 hidden layers with 75 neurons per layer. The loss weights were $w_{\text{PDEs}} = w_{\text{M}} = 10^{-4}$ and $w_{\text{D}} = 1$. The learning rate decay was set to 10^{-3} with a decay rate of 0.95 every 15,000 iterations. The neural networks were trained using the Adam optimizer for 1,000,000 iterations. The total training loss decreased from $\mathcal{O}(10^3)$ to $\mathcal{O}(10^{-3})$, as shown in Fig. 4B.

Unlike the previous example, in which the pressure condition was included in the PINN training, we omitted the pressure information from the training process in this example to evaluate the capability of estimating the material parameters of PINNs with limited information when the force is unknown. While the relative errors of the estimated values were higher in this example, due to both the increased complexity in the model geometry and limited information on the applied load, the parameters of the material estimated by PINN were still in excellent agreement with the ground truth, as shown in Fig. 3C. The search range of E and ν were constrained to the range of [1.5, 7.5] N/mm² and [0, 0.5], respectively. The mean and standard deviation values of E and ν from 10 repeated tests were 5.093 ± 0.107 N/mm² and 0.306 ± 0.008 , respectively. The average runtime in this example was 1.68 hours. The relative errors of the average E and ν were 1.878% and 2.052%, respectively.

2.4.3 Finite element verification

The displacements and principal stresses between the ground truth and verification results are shown in Fig. 4D. These results were obtained using FEA, where the exact solution was generated using the pre-defined material parameters stated in Section. 2.4.1, and the PINN-verification was simulated using

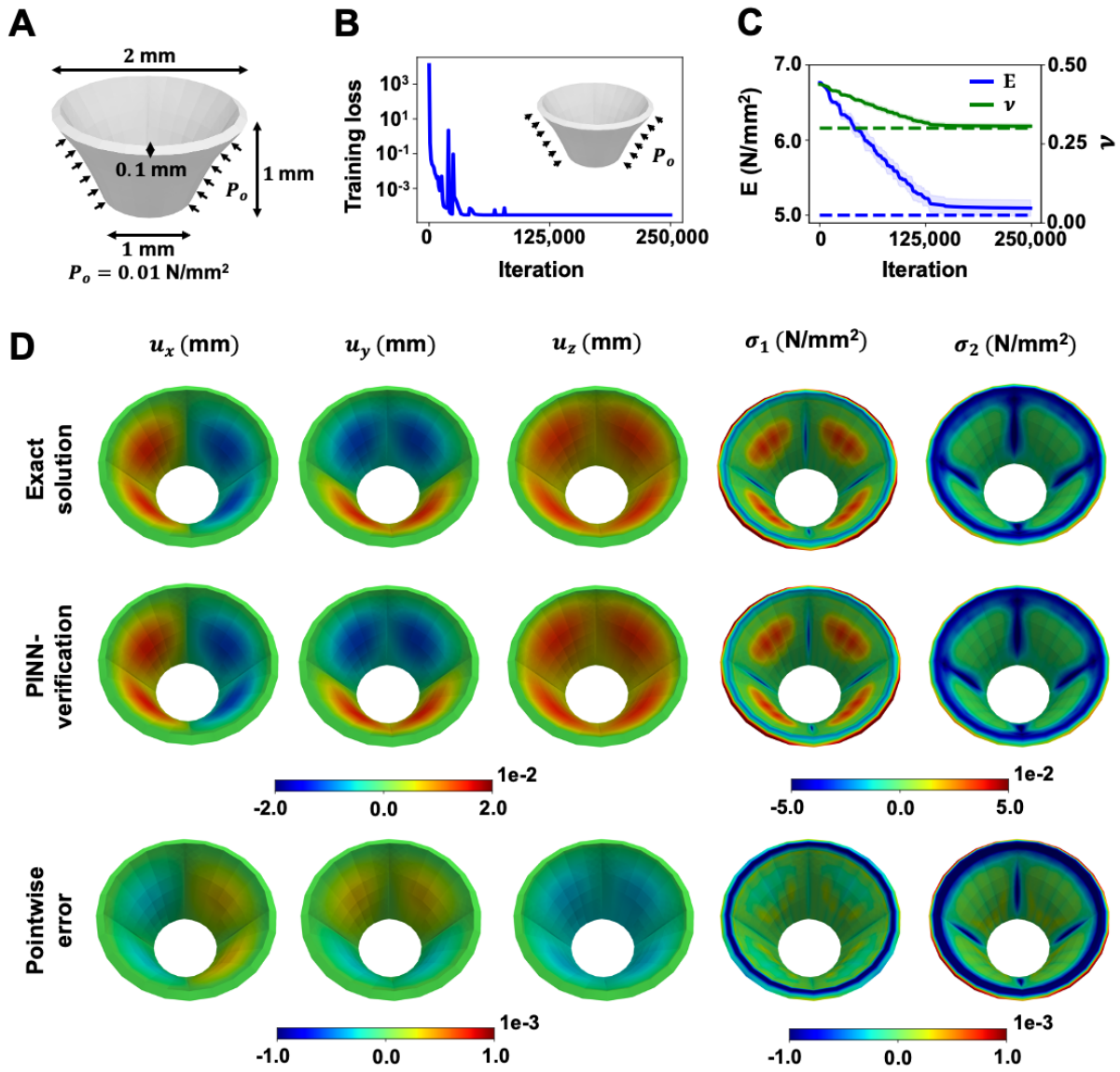


Figure 4. 3D truncated cone verification results. (A) A hollow 3D truncated cone is shown. The cone is 1 mm tall and 0.1 mm thick. The diameters of the top and bottom end are 2 mm and 1 mm, respectively. A uniform external pressure of 10^{-2} N/mm^2 is applied to the outer surface of the cone, with pinned boundary conditions assumed at the top edge of the cone. (B) The total training loss converges rapidly from $\mathcal{O}(10^3)$ to $\mathcal{O}(10^{-3})$ at the end of the analysis. (C) The relative errors of the PINN-estimated E and ν (solid lines) were found to be 1.878% and 2.052%, respectively. (D) The estimated E and ν produced highly accurate displacement and stress fields with less than 3.5% L^2 relative errors between the displacement components and less than 1.5% L^2 relative errors across the principal stress components.

the PINN-estimated parameters indicated in Fig. 4C. The finite element model of the cone was discretized in 11,520 hexahedron elements and analyzed through quasi-static analysis.

As shown in Fig. 4D, the estimated displacements and principal stresses demonstrate strong alignment with the exact solution, with pointwise errors within the range of $\mathcal{O}(10^{-3})$. The L^2 relative errors for u_x , u_y , and u_z were found to be 2.306%, 2.304%, and 3.103%, respectively; the verification results had lower displacement extrema compared to the exact solution. In addition, the L^2 relative error for the first

principal stress (σ_1) was 1.022%, and for the second principal stress (σ_2) was 0.746%. The highest errors in stresses were observed at the top edge where the pinned boundary conditions were applied.

2.5 3D Image-derived tricuspid valve subjected to ventricular pressure

2.5.1 Problem description

Finally, we applied our PINN model to a patient-specific tricuspid valve. The diastolic geometry of the tricuspid valve (Fig. 5A) was segmented from the 3D TEE images of an 11-year-old patient with HLHS. Due to the rapid leaflet motion occurred in the transitioning phase, the strong-form dynamic momentum equation, $\sigma_{ij,j} = \rho \frac{\delta^2 u_i}{\delta t^2}$, was the governing PDE. Here, σ_{ij} denotes the Cauchy stress (we derived Cauchy stress from the first Piola-Kirchhoff stress to maintain consistent notation in our work), ρ denotes material density, u_i is displacement, and t is time. Transvalvular pressure of 97 mmHg was applied to the ventricular surface of the tricuspid valve. The coefficients within the isotropic Neo-Hookean (E and ν) and Lee-Sacks material hyperelastic models (c_0 , c_1 , and c_2) were determined to characterize the elastic properties of the leaflets.

Forward FEA was sought to validate the estimated Neo-Hookean and Lee-Sacks elastic parameters. The annulus displacements derived from image registration were used to enforce annulus dynamic motion. Due to the challenges of identifying the chordae tendineae from 3DE images, we followed a similar chordal projection scheme as described in Wu et al.³³ However, in the current work, the chordae tendineae were modeled as linear elastic trusses, as opposed to springs, with a cross-sectional area of 0.8 mm², an average Young's modulus of 20 MPa, and a Poisson's ratio of 0.3⁴⁸. The tips of the papillary muscles assumed a pinned boundary condition. The resulting leaflet deformation from each material model was compared with the reference segmentation model to validate the accuracy of the estimated elastic parameters.

2.5.2 Estimated results from PINNs

In this example, the same network architecture as in the previous example was used. The leaflet deformation and net stress resulting from the ventricular pressure and chordal reaction forces were output from the parallel FNNs. In the Neo-Hookean PINN model, the loss weights were $w_{\text{PDEs}} = w_{\text{M}} = 10$ and $w_{\text{D}} = 1$. The learning rate decay was set to 10^{-3} with a decay rate of 0.6 every 15,000 iterations. In the Lee-Sacks PINN model, the loss weights were $w_{\text{PDEs}} = w_{\text{M}} = 10^{-4}$ and $w_{\text{D}} = 1$. The learning rate decay was set to 10^{-3} with a decay rate of 0.5 every 15,000 iterations. We trained the neural networks using the Adam optimizer for 250,000 iterations. The loss term associated with the reference displacement data was minimized using the mean symmetric distance metric.

In the Neo-Hookean model, the mechanical properties E and ν were constrained to a broad range of [0, 800] kPa and [0, 0.5], respectively. The mean and standard deviation values of E and ν from 10 repeated tests converged 526.84 ± 47.88 kPa and 0.317 ± 0.021 (Fig. 5B). In the Lee-Sacks, the mechanical properties c_0 , c_1 , and c_2 were constrained to [0, 200] kPa, [0, 200] kPa, and [0, 20], respectively. The approximated mean and standard deviation values of c_0 , c_1 , and c_2 from 10 repeated tests were 165.57 ± 4.01 kPa, 18.68 ± 10.74 kPa, and 2.09 ± 1.25 (Fig. 5C).

2.5.3 Finite element verification

Valve closure was simulated using material parameters estimated by PINNs. Fig. 5D shows the simulated systolic tricuspid valve superimposed on the medical image at four cross-sectional planes. As illustrated, we observed a high degree of overlap between the simulated tricuspid valve (Neo-Hookean in light green and Lee-Sacks in light yellow) and the pixels associated with valve leaflets on the 3D TEE images. The mean symmetric distance between the registration and FE-simulated systolic models was 0.972 mm using Neo-Hookean material model and 0.969 mm for the Lee-Sacks material model. Both values fell within the

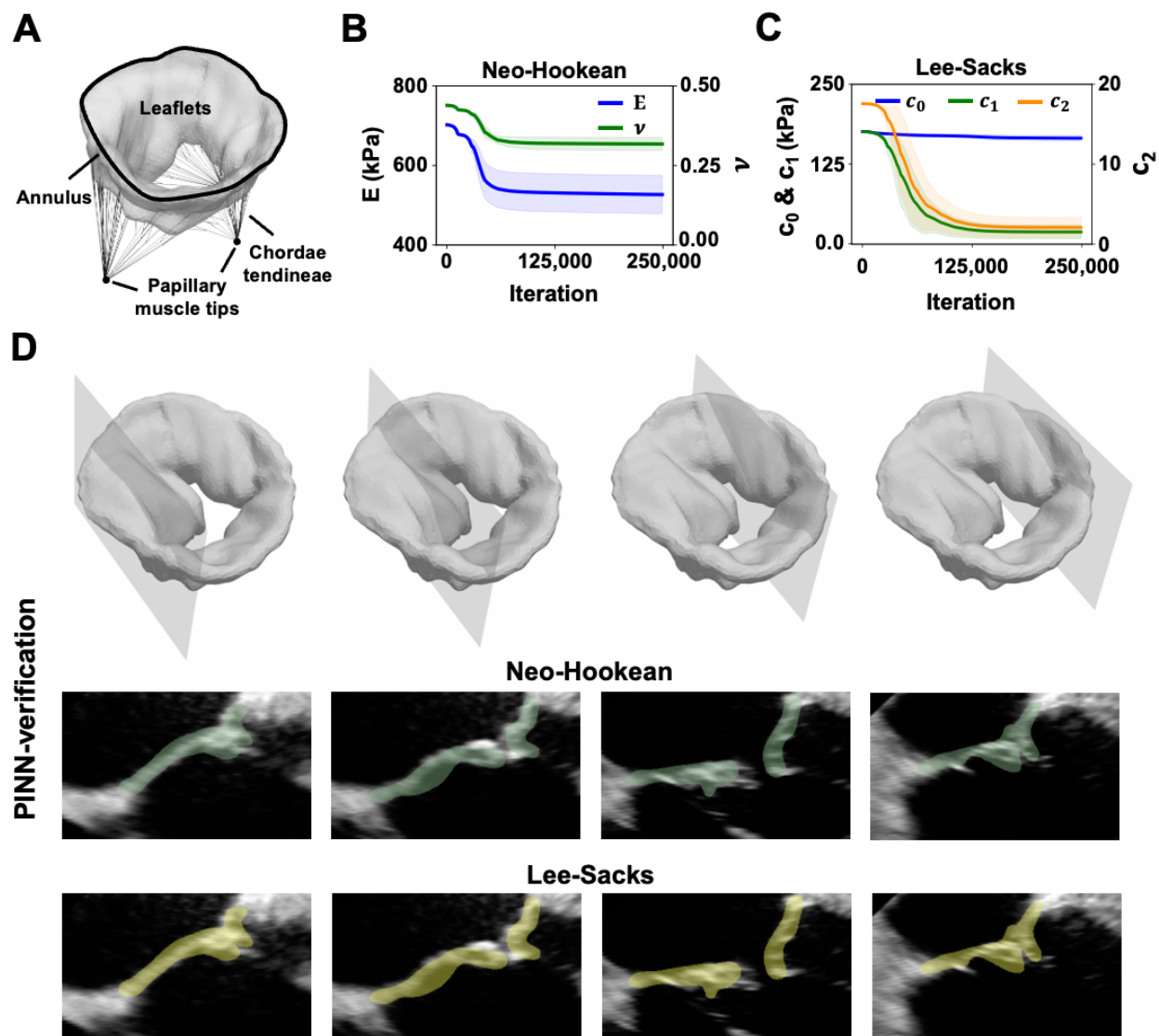


Figure 5. HLHS TV verification results. (A) A 3D image-derived patient-specific tricuspid valve geometry is shown. The valve leaflet geometry and papillary muscle tips were identified from 3D echocardiographic images of the tricuspid valve of an 11-year-old patient with hypoplastic left heart syndrome in 3D Slicer. A total of 69 branch chords were projected from the papillary muscle tips to a chordae insertion zone defined from the free edge to mid-height of the tricuspid valve. A uniform transvalvular pressure of 97 mmHg was applied to the ventricular surface of the tricuspid valve. (B) The mean and standard deviation of the estimated E and ν in the Neo-Hookean model were 526.84 ± 47.88 kPa and 0.317 ± 0.021 at the final analysis step. (C) The mean and standard deviation of the estimated c_0 , c_1 , and c_2 in the Lee-Sacks model from 10 repeated tests were 165.57 ± 4.01 kPa, 18.68 ± 10.74 kPa, and 2.09 ± 1.25 , respectively. (D) The simulated systolic tricuspid valve produced excellent agreement when overlaid on top of the medical image (in light green for the Neo-Hookean model and light yellow for the Lee-Sacks model) The mean symmetric distance between the reference segmentation model and FE-simulated systole model was 0.972 mm using Neo-Hookean material model and 0.969 mm for the Lee-Sacks material model.

range of inter-observer variability observed for manual segmentation reported in the literature⁴⁹. The 95th percentile Hausdorff distance resulting from the Neo-Hookean and Lee-Sacks models were 3.10 mm and 3.22 mm. These similarity metrics were computed from a Python script.

2.5.4 Uncertainty analysis

Taking the standard deviation of the estimated elastic parameters from the 10 repeated PINN experiments, we performed a sensitivity analysis to assess the effect of variations in each of the elastic parameters on the 95th percentile (%ile) first principal stress (σ_1), strain (ϵ_1) and Hausdorff distance, as well as the mean symmetric distance. Fig. 6A-C are sensitivity analysis results generated for the Neo-Hookean model, and Fig. 6D-F are the Lee-Sacks model. Fig. 6A and D show the distribution of σ_1 and ϵ_1 on the atrial surface of the tricuspid valve. These profiles were simulated using the mean Neo-Hookean elastic parameters (*i.e.*, E_{mean} and ν_{mean}) and Lee-Sacks elastic parameters (*i.e.*, $c_{0,\text{mean}}$, $c_{1,\text{mean}}$, $c_{2,\text{mean}}$), respectively. Qualitatively, both material models produced similar stress and strain patterns, with higher tensile stress and strain observed on the anterior leaflet compared to the other two leaflets. Quantitatively, the 95th %ile σ_1 and ϵ_1 resulting from the Neo-Hookean model were 75.02 kPa and 0.18 and from the Lee-Sacks model were 80.91 kPa and 0.19.

We used a Python subroutine called FEBioUncertainSCI^{50,51} to calculate sensitivity of the 95th %ile σ_1 , 95th %ile ϵ_1 , 95th %ile Hausdorff distance, and mean symmetric distance in the tricuspid valve with respect to variations in elastic parameters. Interested readers may refer to^{50,51} on the theoretical background supporting the parametric uncertainty quantification method in UncertainSCI. In the Neo-Hookean example, we randomly generated 20 pairs of E and ν in a 2-dimensional space bounded by $E_{\text{mean}} \pm E_{\text{std}}$ and $\nu_{\text{mean}} \pm \nu_{\text{std}}$ using a third order polynomial chaos expansion (PCE) function to build a PCE emulator. We performed a FEA for each pair of E and ν to approximate their corresponding σ_1 , ϵ_1 , Hausdorff distance, and mean symmetric distance. These input and output variables were then used to train a PCE emulator to generate a manifold of total sensitivity indices between each permutation of the input and output parameters. The total sensitivity indices measure the combined direct effects of individual parameters (first-order sensitivity) and their fractional contributions resulting from higher-order parameter interactions (second or higher-order sensitivity) on the variance of model output parameters.

The total sensitivity indices at the 95th %ile of σ_1 , ϵ_1 , the Hausdorff distance, and the mean symmetric distance in the Neo-Hookean model are provided in Fig. 6B. As shown, within the sampling space, E had significantly higher total-order sensitivity indices in ϵ_1 , Hausdorff distance, and mean symmetric distance, indicating its dominant role in influencing the kinematics behaviors of the tricuspid valve. In the context of σ_1 , the sensitivity indices were comparable between E and ν , with ν had a slightly higher influence. We queried 10^3 sampling pairs of E and ν from the PCE emulator. Fig. 6C presents raincloud plots that illustrate the key statistics (*e.g.*, minimum, maximum, median) as well as the distribution of these 10^3 E and ν pairs on each output metric. Overall, we observed a narrow range of the maximum and minimum values in each output metric, except for the 95th %ile ϵ_1 , where the percentage difference between the maximum and minimum values well exceeded 10%. This indicates that strain prediction has the highest uncertainty with respect to changes in E and ν among the metrics.

In the Lee-Sacks example, we built a PCE emulator on 30 randomly sampled sets of c_0 , c_1 , and c_2 in a 3-dimensional space bounded by $c_{0,\text{mean}} \pm c_{0,\text{std}}$, $c_{1,\text{mean}} \pm c_{1,\text{std}}$, and $c_{2,\text{mean}} \pm c_{2,\text{std}}$ and their corresponding σ_1 , ϵ_1 , Hausdorff distance, and mean symmetric distance. The total sensitivity indices at the 95th %ile of σ_1 , ϵ_1 , the Hausdorff distance, and the mean symmetric distance are provided in Fig. 6E. Overall, within this sampling space, c_2 appeared to have the highest influence on the 95th %ile of σ_1 , ϵ_1 , and the mean symmetric distance. Contrarily, c_0 had a higher sensitivity index at the 95th %ile of Hausdorff distance. The distributions of each output metric from 10^3 sampling pairs of c_0 , c_1 , and c_2 are shown in Fig. 6F. Higher uncertainties in the 95th %ile of σ_1 and ϵ_1 were observed, with more than 10% difference between the maximum and minimum values of the metrics. However, the differences between the extrema were negligible in the 95th %ile Hausdorff distance and mean symmetric distance.

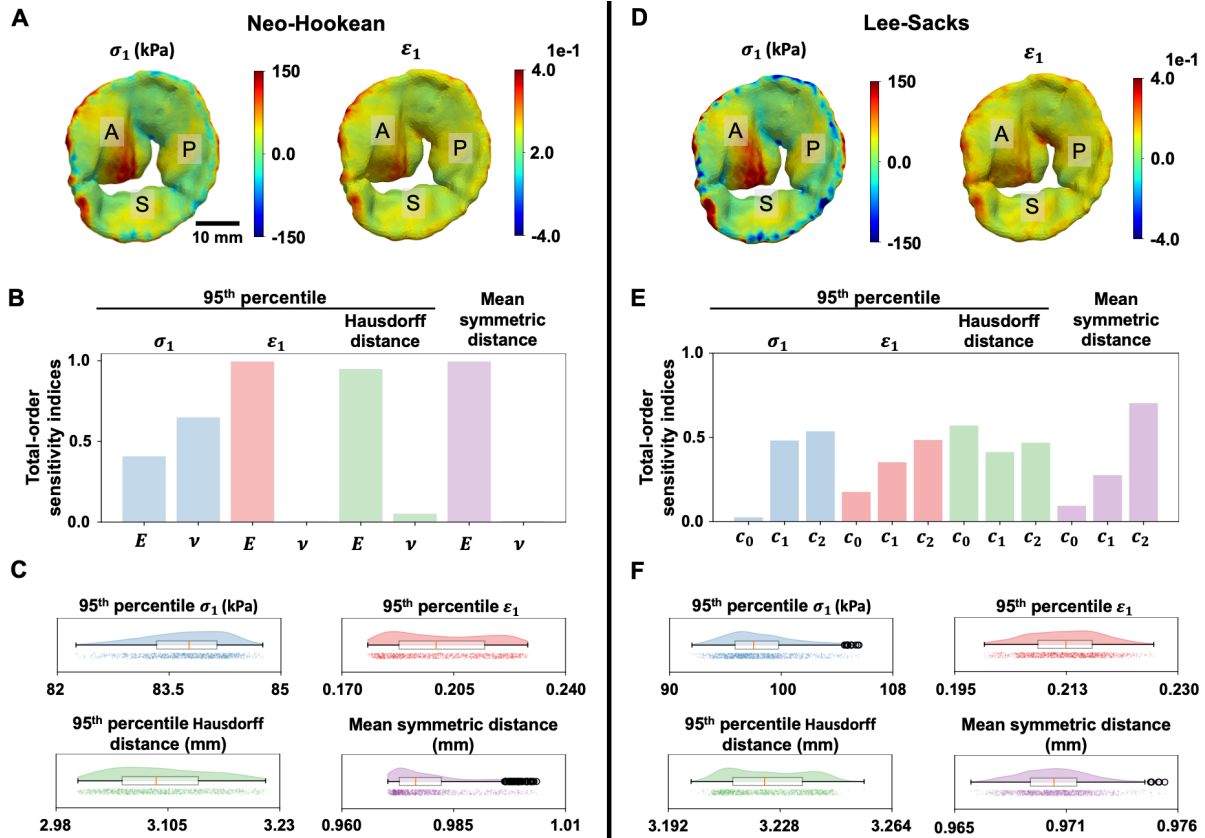


Figure 6. HLHS TV sensitivity analysis results. The first principal stress (σ_1) and strain (ϵ_1) simulated using the mean Neo-Hookean elastic parameters (A) and Lee-Sacks elastic parameters (D) are shown. A higher tensile stress and strain are observed on the anterior leaflet on both models. The 95th %ile σ_1 and ϵ_1 resulting from the Neo-Hookean model are 75.02 kPa and 0.18 and from the Lee-Sacks model were 80.91 kPa and 0.19. In the Neo-Hookean model, (B) variations in E have bigger effects on ϵ_1 , Hausdorff distance, and mean symmetric distance, while variations in ν have a bigger effect on σ_1 . (C) The percentage difference between the extrema is well above 10% in ϵ_1 , indicating that strain prediction has the highest uncertainty with respect to changes in E and ν among the metrics. The ranges between the extrema in other output metrics are relatively narrow. In the Lee-Sacks model, (E) c_2 has the highest influence on the 95th %ile of σ_1 , ϵ_1 , and the mean symmetric distance, while c_0 has a higher sensitivity index at the 95th %ile of Hausdorff distance. (F) σ_1 and ϵ_1 demonstrate higher uncertainty, with more than 10% difference between their extrema. However, the differences between the extrema are negligible in the Hausdorff distance and mean symmetric distance.

3 Discussion

We have developed a noninvasive approach to characterize the elastic properties of heart valve tissues using *in vivo* 4D images. Our approach consists of two steps. First, deformable image registration was used to estimate the spatial displacements of valve leaflets from echocardiogram data. Subsequently, PINN was applied to infer the elastic parameters from image-derived displacement and the governing principles of the system. We evaluated the robustness of PINN on a series of simplified benchmarks prior to applying our framework to the challenge case, the tricuspid valve of a child. In the benchmark problems, PINN successfully determined the “unknown” elastic parameters with satisfactory accuracy of within 3% of L^2 relative errors compared to the ground truth. In the patient-specific tricuspid valve application, where the exact *in vivo* material properties of valve tissue are unknown, a forward FEA was performed to simulate valve closure using the estimated tissue elastic parameters. Material parameters for the Neo-Hookean and Lee-Sacks constitutive models were identified. The resulting closed valve geometries were within 1 mm

mean symmetric distance compared to the segmentation ground truth. This error is within the range of those reported in the literature in the context of interobserver variability in manual valve modeling⁴⁹.

There has been a long-standing interest in *in vivo* heart valve biomechanics research due to the strong implication and relevance of valve mechanics to the pathogenesis, progression, and repair of heart valves^{52–54}. Numerous methods have been proposed to estimate *in vivo* leaflet strain and valve dynamics to understand changes in strain between healthy and disease states, as well as between pre- and post-repair states^{32,55–57}. These retrospective studies are valuable for relating leaflet strain to valve function and identifying the functional characteristics of heart valves. Moving forward, it is equally imperative to develop the capability for prognostic studies to predict disease progression and to determine optimal repair options to reduce long-term patient morbidity and mortality^{27,29}. Our proposed approach provides a risk-free platform for clinicians to simulate outcomes of virtual intervention prior to performing surgery or intervention on actual patients^{25,58,59}. Our framework, which we have named ADEPT, enables accurate identification of *in vivo* elastic properties of valve tissue unique to each patient. This new capability offers the future potential to facilitate personalized virtual intervention analysis and use simulated models to identify the most effective repair option rather than clinical intuition alone. Due to the wide range of tissue extensibility from neonates to adults^{60,61}, and the considerable heterogeneity in valve structure⁹, this approach holds particular significance for application to patients with congenital heart disease.

Traditionally, inverse FEA has been a common approach to characterize *in vivo* elastic properties of heart valve tissues^{48,62}. In these previous studies, physical markers were sutured to the leaflets to measure the actual leaflet displacements. Subsequently, FEA was performed iteratively to identify an optimal set of tissue stiffness parameters that provides agreeable simulated displacements compared to the measured ones. Of the studies, Rausch et al.⁶² found elastic parameters of $c_0 = 35.9$ kPa, and weighting factors of $c_1 = 2.3$ and $c_2 = 9.8$ using a coupled anisotropic model provide the most agreeable *in vivo* behavior approximation of a mitral valve anterior leaflet. Krishnamurthy et al.⁴⁸ performs inverse studies on 17 ovine anterior leaflets using a three-parameter orthotopic linear elastic model and found the elastic parameters to be $E_{\text{circ}} = 43 \pm 18$ kPa, $E_{\text{rad}} = 11 \pm 3$ kPa and $G_{\text{circ-rad}} = 121 \pm 22$ kPa. In our work, we furnished a noninvasive approach that combines deformable image registration and PINN to identify *in vivo* tissue properties using clinically acquired 3D images. In our patient-specific analysis, the elastic parameter within an isotropic Neo-Hookean model was found to be 526.84 ± 47.88 kPa. Additionally, the elastic parameters within an isotropic Lee-Sacks model were found to be $c_0 = 165.57 \pm 4.01$ kPa, $c_1 = 18.68 \pm 10.74$ kPa, and $c_2 = 2.09 \pm 1.25$ kPa. Although elastic parameters in different constitutive models hold different influence on the concavity of the stress-strain curve, our results were of similar magnitude to the previously reported values.

In previous analyses of tricuspid valves, Stevanella et al.⁶³ reports a maximum 1st principal stress of 430 kPa⁶³ and circumferential and radial strains of 0.13–0.16 and 0.25–0.30 on the anterior leaflet belly at 23 mm Hg transvalvular pressure. Kong et al.²⁵ reports 1st principal stress in the range of 24–91 kPa and 1st principal strain in the range of 0.07 to 0.21 at mid-systole under the same peak transvalvular pressure. In our example, due to systemic right ventricle in the 11-year-old patient, the tricuspid valve was subjected to a 97 mm Hg transvalvular pressure, a pressure loading close to that experienced by a mitral valve. To offer additional references on mitral valve stress and strain, Wang et al.⁶⁴ reported 160 kPa maximum principal stress at 110 mm Hg peak systolic pressure. Lee et al.⁶⁵ found a maximum radial and circumferential stresses of 509.5 ± 38.4 kPa and 301.4 ± 12.2 kPa on the anterior leaflet at 90 mm Hg peak transvalvular pressure. Furthermore, Rausche et al.⁶⁶ found a maximum principal strains of 0.13 ± 0.047 in ovine leaflets. Our *in vivo* analysis produced a maximum 1st principal stress and strain around 75.02 kPa and 0.18 using a Neo-Hookean model, and 80.91 kPa and 0.19 using a Lee-Sacks model, which are within the range of those reported by Kong et al.²⁵. Qualitatively, our findings are in line with the literature as we

also observed highest 1st principal stress and strain located on the anterior leaflet. The exact stress and strain values are likely affected by a combination of factors including valve morphology, transvalvular pressure, and the chosen material model. It is possible that the lower principal values found in our study are attributed to the smaller valve size in our patient compared to that in an adult. Nonetheless, our strain values are in close alignment with existing literature reporting.

Notably, the combination of patient specific leaflet structure and material properties will be powerful, additional challenges to truly patient specific modeling remain including resolving leaflet chordal insertions. Current cine *in vivo* imaging modalities can reliably visualize the papillary muscles (where chordae tendineae emanate from the ventricular myocardium), but not individual chordal insertions at the level of the valve leaflets themselves²⁷. However, previous work by Khaligi et al.²⁴ demonstrates that functional equivalent chordal models can be created. As such, while chordae insertion locations may influence the local stress and strain distribution, functional equivalence can yield accurate leaflet deformation, as demonstrated in our analysis. Unlike Khaligi et al., a more realistic branching chordal model is utilized in the present work. The effects of chordae density, length, and insertion sites on the resulting stress, strain, regurgitation orifice area, and leaflet contact areas of atrioventricular valves are areas for further investigation.

4 Conclusions

We presented a noninvasive approach to identify *in vivo* elastic properties of valve tissue from 4D medical images using deformable image registration and rigorously verified PINN models. The estimated elastic parameters and consequent leaflet deformation, stresses, and strains are in excellent agreement with reference solutions and values reported in the literature. While our work directly benefits the development of patient-specific computer simulations of heart valve mechanics and repairs, the idea of combining image registration and PINNs to determine elastic properties of soft tissue noninvasively, whether for diagnostic or prognostic purposes, is broadly applicable to a wide spectrum of cardiovascular structures and beyond.

5 Methods

This section provides the background and technical details of deformable registration, PINNs, and computational solid mechanics pertaining to the noninvasive method of identifying material parameters proposed in the current work.

5.1 Image processing

Here, we outline the image analysis process to acquire patient-specific geometry and displacement fields of the tricuspid valve. All image processing tasks were performed using open-source image analysis platforms, 3D Slicer⁶⁷, SlicerHeart⁶⁸, and Greedy deformable image registration³⁴.

5.1.1 Image acquisition

The 3D transesophageal (TEE) images of a regurgitant tricuspid valve were identified from an existing database at the Children's Hospital of Philadelphia. The images were acquired on a Philips Epiq system (Philips Medical, Boston, MA) from a child with Hypoplastic left heart syndrome (HLHS). HLHS is a complex congenital heart disease that affects more than 1,000 liveborns in the US each year. Patients with HLHS have to undergo three staged open-chest reconstruction surgeries. About twenty-five percent of HLHS patients develop tricuspid regurgitation following the third surgery, which significantly increases their risk of heart failure. The objective of this work is to provide a noninvasive approach to evaluate the mechanical factors that influence valve competency in HLHS patients. This study was approved by

the Institutional Review Board at the Children’s Hospital of Philadelphia. The 3D TEE images were imported into 3D Slicer using the Philips 4D US DICOM patcher module in SlicerHeart^{16,69} for image segmentation and registration.

5.2 Manual image segmentation

The selected 3DE images were manually segmented using the SliceHeart extension 3D Slicer. Specifically, an expert observer manually traced the leaflets of the tricuspid valve in the last diastolic frame of the cardiac cycle. The image voxels that correspond to the leaflets were assigned a label value of 1, and all other voxels had a label of 0. The visible segments (*i.e.*, image voxels with label 1) were converted to a surface model that encapsulates the full 3D geometry of the tricuspid valve. The segmentation model was subsequently meshed with 5000 nodes using the Surface Toolbox module in 3D Slicer to create a smooth representation of the tricuspid valve geometry.

5.3 Deformable image registration

Intensity-based deformable registration was performed on two consecutive cardiac frames (the last diastolic frame and the first systolic frame were chosen for this study) to obtain the deformation fields of the tricuspid valves when fully pressurized. The Greedy diffeomorphic image registration algorithm was used to facilitate deformable registration between the 3DE reference-target image pair³⁴. The image deformation approach performed in this work was inspired by Aggarwal et al.³⁵. In particular, we first defined the registration region of interest (ROI) for the reference frame by dilating the diastolic segmentation of the tricuspid valve with 10 voxels in the x , y , and z directions. To define the registration ROI for the target frame, we roughly approximated the deformation fields by registering the 3DE reference grayscale image at half-resolution and warped the resulting deformation fields to the reference ROI. Finally, we performed full-resolution registration on the grayscale image pair, guided by their respective ROI, to acquire refined deformation fields on the tricuspid valve leaflets.

The Greedy registration framework is inspired by the Large Deformation Diffeomorphic Metric Mapping (LDDMM) formulation presented in⁷⁰. For a given image pair, suppose the reference image is denoted \mathcal{I} , the target image is denoted \mathcal{J} , and a diffeomorphism map that transforms the physical coordinates of image \mathcal{I} into image \mathcal{J} is defined as φ . The diffeomorphism, φ , is obtained by integrating the velocity fields, \mathbf{v}_t , from time t_0 to t_1 defined as

$$\varphi_{t_1} = \varphi_{t_0} + \int_{t_0}^{t_1} \|\mathbf{v}_t\|_L dt,$$

where $\|\cdot\|_L$ is a linear differential operator that regularizes the velocity field, expressed in the form of $L = \alpha \nabla^2 + \beta \mathbf{Id}$. Within linear operator L , \mathbf{Id} is the identity map. α and β are gradient smoothing and deformation field smoothing constants, with assigned values of 2.3mm and 0.35mm, respectively, to ensure good registration alignment while preserving smooth displacement features. The objective is to compute velocity fields, \mathbf{v}_t , such that the image similarity loss, $\mathcal{L}_{\text{sim}}(\varphi\mathcal{I} - \mathcal{J})$, is minimized. The sum of the squared difference similarity measure was used in the present work. The Greedy registration tool shares many similarities with the theoretical framework established in⁷¹, while also incorporating additional image metrics and nonsymmetric deformation implementations to optimize computational efficiency⁷².

5.4 Physics-informed neural networks for material parameter identification

Here, we provide an overview of PINNs and the technical details considered in this work. The PINN architecture was set up using the DeepXDE library³⁷. All PINN experiments were trained on an NVIDIA H100 80GB GPU. The source code will be made available upon publication in the GitHub repository <https://github.com/lu-group/adept>.

5.4.1 Neural network architecture

The PINN architecture is shown in Fig. 1B. Let $\mathcal{N}^L(\mathbf{x}) : \mathbb{R}^{\dim(\mathbf{x})} \rightarrow \mathbb{R}^{\dim(\mathbf{y})}$ be a L -layer neural network that maps input features \mathbf{x} to output feature \mathbf{y} with \mathcal{N}^l neurons in the l -layer. The connectivity between layer l and $l-1$ is governed by $\mathcal{N}^l(\mathbf{x}) = \phi(\mathbf{W}^l \mathcal{N}^{l-1}(\mathbf{x}) + \mathbf{b}^l)$, where ϕ is a nonlinear activation function, \mathbf{W}^l is a weight matrix, and \mathbf{b}^l is a bias vector. We used *swish* activation function and Glorot uniform weight initialization method in all analyses. Given that the activation function is applied element-wise to each neuron, the recursive FNN is defined as:

$$\begin{aligned} \text{input layer : } & \mathcal{N}^0(\mathbf{x}) = \mathbf{x} \in \mathbb{R}^{\dim(\mathbf{x})}, \\ \text{hidden layer } l : & \mathcal{N}^l(\mathbf{x}) = \text{swish}\left(\mathbf{W}^l \mathcal{N}^{l-1}(\mathbf{x}) + \mathbf{b}^l\right) \in \mathbb{R}^{\mathcal{N}^l}, \quad \text{for } 1 \leq l \leq L-1, \\ \text{output layer : } & \mathcal{N}^L(\mathbf{x}) = \mathbf{W}^L \mathcal{N}^{L-1}(\mathbf{x}) + \mathbf{b}^L \in \mathbb{R}^{\dim(\mathbf{y})}. \end{aligned}$$

The nodal coordinates were used as input variables for the network. The network architectures consisted of two independent feedforward networks. One of the independent networks was responsible for estimating displacement fields \mathcal{N}_{u_i} . The other independent network was responsible for estimating the stress fields $\mathcal{N}_{\sigma_{ij}}$. The displacement fields were normalized based on the mean and standard deviation of the ground truth displacement data supplied to improve training efficiency. Within the architecture, θ_{NN} encapsulates network variables \mathbf{W}^l and \mathbf{b}^l , while θ_{mat} contains unknown material variables.

5.4.2 Loss function

In inverse analysis, PINN seeks to optimize the network parameters, θ_{NN} (*i.e.*, \mathbf{W}^l and \mathbf{b}^l), and the unknown material parameters, θ_{mat} (*e.g.*, E and ν) in the training process expressed as

$$\theta_{\text{NN}}^*, \theta_{\text{mat}}^* = \arg \min_{\theta_{\text{NN}}, \theta_{\text{mat}}} \mathcal{L}(\theta_{\text{NN}}, \theta_{\text{mat}}),$$

with the general total loss function $\mathcal{L}(\theta_{\text{NN}}, \theta_{\text{mat}})$ defined as

$$\mathcal{L}(\theta_{\text{NN}}, \theta_{\text{mat}}) = w_{\text{PDEs}} \mathcal{L}_{\text{PDEs}} + w_{\text{M}} \mathcal{L}_{\text{M}} + w_{\text{F}} \mathcal{L}_{\text{F}} + w_{\text{D}} \mathcal{L}_{\text{D}}.$$

Herein, w_{\bullet} represents the weight associated with its corresponding loss term \mathcal{L}_{\bullet} . \mathcal{L}_{M} , \mathcal{L}_{F} , and \mathcal{L}_{D} refer to errors in material constitutive relations, traction balance, and displacement reference data, respectively. The strong form of the momentum equation was selected as the governing PDEs. The Dirichlet conditions were implicitly enforced in the PDE approximation as hard constraint conditions. Note that the traction loss was only considered in example 1. All other examples were trained without enforcing force balance to evaluate the robustness of our approach in settings where the underlying physics was only partially known.

In examples 1–3, all loss terms were optimized using mean squared errors. In example 4, the loss term \mathcal{L}_{D} was optimized by mean symmetric distance as image intensity-derived displacement fields may differ from the displacement fields derived from material point frame of reference in continuum mechanics⁷³. Suppose we have two finite point sets, P and R , the mean symmetric distance is defined as

$$\mathcal{L}_{\text{D}} = \frac{1}{2} \left(\frac{1}{|P|} \sum_{p \in P} \min_{r \in R} \|p - r\| + \frac{1}{|R|} \sum_{r \in R} \min_{p \in P} \|p - r\| \right).$$

The mean symmetric distance measures the average minimum distance from P to R and from R to P . Here, $\|\cdot\|$ denotes the Euclidean distance. The point sets P and R represent the deformed nodal coordinates of the tricuspid valve at systole estimated in PINNs and derived from image registration, respectively.

5.5 Material constitutive models

Various material constitutive models were tested in the examples presented in this work. The benchmark examples detailed in Sections 2.2 to 2.4 assumed an isotropic linear elastic material model. For the patient-specific tricuspid valve described in Section 2.5, isotropic Neo-Hookean and Lee-Sacks material models were applied.

Linear elastic model. The isotropic linear elastic material constitutive model is defined as:

$$\boldsymbol{\sigma} = \mathbf{C} \cdot \boldsymbol{\varepsilon},$$

with

$$\boldsymbol{\sigma} = \begin{bmatrix} \sigma_{xx} \\ \sigma_{yy} \\ \sigma_{xy} \end{bmatrix}; \quad \mathbf{C} = \frac{E}{(1-\nu^2)} \begin{bmatrix} 1 & \nu & 0 \\ \nu & 1 & 0 \\ 0 & 0 & (1-\nu) \end{bmatrix}; \quad \boldsymbol{\varepsilon} = \begin{bmatrix} \varepsilon_{xx} \\ \varepsilon_{yy} \\ \varepsilon_{xy} \end{bmatrix}.$$

In the 2D thick-walled cylinder and 3D truncated cone examples, the kinematic relations are expressed as:

$$\varepsilon_{xx} = \frac{\partial u_x}{\partial x}; \quad \varepsilon_{yy} = \frac{\partial u_y}{\partial y}; \quad \varepsilon_{xy} = \frac{1}{2} \left[\frac{\partial u_x}{\partial y} + \frac{\partial u_y}{\partial x} \right].$$

In the deflected circular plate example, $u_x = -z \frac{\partial u_z}{\partial x}$ and $u_y = -z \frac{\partial u_z}{\partial y}$. Therefore, the kinematic relations are

$$\varepsilon_{xx} = -z \frac{\partial^2 u_z}{\partial x^2}; \quad \varepsilon_{yy} = -z \frac{\partial^2 u_z}{\partial y^2}; \quad \varepsilon_{xy} = -z \frac{\partial^2 u_z}{\partial x \partial y}.$$

Neo-Hookean model. The Neo-Hookean model⁷⁴ is developed to characterize the behavior of nonlinear materials that undergo deformations. Within this model, the strain energy density function, Ψ , is defined as

$$\Psi(I_1, J) = \frac{1}{2} \lambda [\log(J)]^2 - \mu \log(J) + \frac{1}{2} \mu (I_1 - 3),$$

where I_1 is the first principal invariants denoted as $I_1 = \text{trace}(\mathbf{F}^T \cdot \mathbf{F})$, \mathbf{F} is the deformation gradient denoted as $F_{ij} = \delta_{ij} + u_{i,j}$, u_i is the displacement vector, and λ and μ are the Lamé's elasticity parameters. The first Piola-Kirchhoff stress is given by

$$\mathbf{P} = \frac{\partial \Psi}{\partial \mathbf{F}} = \mu \mathbf{F} + [\lambda \log(J) - \mu] \mathbf{F}^{-T}.$$

where

$$\lambda = \frac{E\nu}{(1+\nu)(1-2\nu)}, \quad \text{and} \quad \mu = \frac{E}{2(1+\nu)}.$$

Lee-Sacks model. The Lee-Sacks isotropic material model⁶⁵ is a popular model for characterizing heart valve tissue properties. It combines Neo-Hookean with an exponential term to account for contributions of the extracellular matrix and collagen fiber network in leaflet tissues. The hyperelastic strain energy function is expressed as

$$\Psi(I_1) = \frac{c_0}{2} (I_1 - 3) + \frac{c_1}{2} \{ \exp [c_2 (I_1 - 3)^2] - 1 \},$$

where c_0 , c_1 , and c_2 are stiffness parameters. The first Piola-Kirchhoff stress is given by

$$\mathbf{P} = \frac{\delta \Psi}{\delta \mathbf{F}} = (c_0 + 2c_1 c_2 (I_1 - 3) \exp [c_2 (I_1 - 3)^2]) \mathbf{F}.$$

Acknowledgments

This work was supported by the Cora Topolewski Pediatric Valve Center at the Children's Hospital of Philadelphia, an Additional Ventures Expansion Award, the National Institutes of Health (NIGMS 2R01GM083925, NHLBI T32 HL007915, NHLBI K25 HL168235, NHLBI R01 HL153166, NHLBI R01 HL163202), the U.S. Department of Energy (Grants No. DE-SC0025592 and No. DE-SC0025593), and the National Science Foundation (Grant No. DMS-2347833). The authors thank the CHOP Research Institute for generously providing the GPU resources necessary to support this project.

References

1. Coffey, S. *et al.* Global epidemiology of valvular heart disease. *Nat. Rev. Cardiol.* **18**, 853–864, DOI: <https://doi.org/10.1038/s41569-021-00570-z> (2021).
2. Santangelo, G. *et al.* The global burden of valvular heart disease: From clinical epidemiology to management. *J Clin Med* **12**, DOI: <https://doi.org/10.3390/jcm12062178> (2023).
3. Tseng, S. Y. *et al.* Atrioventricular valve regurgitation in single ventricle heart disease: A common problem associated with progressive deterioration and mortality. *J. Am. Hear. Assoc.* **9**, e015737, DOI: <https://doi.org/10.1161/JAHA.119.015737> (2020).
4. Arnaert, S. *et al.* Heart failure related to adult congenital heart disease: prevalence, outcome and risk factors. *ESC Hear. Fail.* **8**, 2940–2950, DOI: <https://doi.org/10.1002/ehf2.13378> (2021).
5. Hensey, M. *et al.* Transcatheter mitral valve replacement. *JACC: Cardiovasc. Interv.* **14**, 489–500, DOI: <https://doi.org/10.1016/j.jcin.2020.12.038> (2021).
6. Buratto, E. & Konstantinov, I. E. Atrioventricular valve surgery: Restoration of the fibrous skeleton of the heart. *J Thorac Cardiovasc. Surg* **162**, 360–365, DOI: <https://doi.org/10.1016/j.jtcvs.2021.03.128> (2021).
7. Levack, M. M. *et al.* Three-dimensional echocardiographic analysis of mitral annular dynamics. *Circulation* **126**, S183–S188, DOI: <https://doi.org/10.1161/CIRCULATIONAHA.111.084483> (2012).
8. Salgo, I. S. *et al.* Effect of annular shape on leaflet curvature in reducing mitral leaflet stress. *Circulation* **106**, 711–717, DOI: <https://doi.org/10.1161/01.CIR.0000025426.39426.83> (2002).
9. Nam, H. H. *et al.* Modeling of the tricuspid valve and right ventricle in hypoplastic left heart syndrome with a fontan circulation. *Circ. Cardiovasc. Imaging* **16**, e014671, DOI: <https://doi.org/10.1161/CIRCIMAGING.122.014671> (2023).
10. Bouma, W. *et al.* Preoperative three-dimensional valve analysis predicts recurrent ischemic mitral regurgitation after mitral annuloplasty. *Ann Thorac Surg* **101**, 567–575, DOI: <https://doi.org/10.1016/j.athoracsur.2015.09.076> (2016).
11. Wijdh-den Hamer, I. J. *et al.* The value of preoperative 3-dimensional over 2-dimensional valve analysis in predicting recurrent ischemic mitral regurgitation after mitral annuloplasty. *J Thorac Cardiovasc. Surg* **152**, 847–859, DOI: <https://doi.org/10.1016/j.jtcvs.2016.06.040> (2016).
12. Lee, A. P.-W. *et al.* Quantitative analysis of mitral valve morphology in mitral valve prolapse with real-time 3-dimensional echocardiography. *Circulation* **127**, 832–841, DOI: <https://doi.org/10.1161/CIRCULATIONAHA.112.118083> (2013).
13. Grewal, J. *et al.* Mitral annular dynamics in myxomatous valve disease. *Circulation* **121**, 1423–1431, DOI: <https://doi.org/10.1161/CIRCULATIONAHA.109.901181> (2010).

14. Nam, H. H. *et al.* Dynamic annular modeling of the unrepaired complete atrioventricular canal annulus. *Ann Thorac Surg* **113**, 654–662, DOI: <https://doi.org/10.1016/j.athoracsur.2020.12.013> (2022).
15. Nam, H. H. *et al.* Visualization and quantification of the unrepaired complete atrioventricular canal valve using open-source software. *J Am Soc Echocardiogr* **35**, 985–996, DOI: <https://doi.org/10.1016/j.echo.2022.04.015> (2022).
16. Nguyen, A. V. *et al.* Dynamic three-dimensional geometry of the tricuspid valve annulus in hypoplastic left heart syndrome with a fontan circulation. *J. Am. Soc. Echocardiogr.* **32**, 655–666.e13, DOI: <https://doi.org/10.1016/j.echo.2019.01.002> (2019).
17. Colen, T. *et al.* Tricuspid valve adaptation during the first interstage period in hypoplastic left heart syndrome. *J Am Soc Echocardiogr* **31**, 624–633, DOI: <https://doi.org/10.1016/j.echo.2017.11.020> (2018).
18. Kutty, S. *et al.* Tricuspid regurgitation in hypoplastic left heart syndrome. *Circ. Cardiovasc. Imaging* **7**, 765–772, DOI: <https://doi.org/10.1161/CIRCIMAGING.113.001161> (2014).
19. Asmarats, L., Puri, R., Latib, A., Navia, J. L. & Rodés-Cabau, J. Transcatheter tricuspid valve interventions. *J. Am. Coll. Cardiol.* **71**, 2935–2956, DOI: <https://doi.org/10.1016/j.jacc.2018.04.031> (2018).
20. Del Forno, B. *et al.* Mitral valve regurgitation: a disease with a wide spectrum of therapeutic options. *Nat. Rev. Cardiol.* **17**, 807–827, DOI: <https://doi.org/10.1038/s41569-020-0395-7> (2020).
21. Narang, H. *et al.* Pre-surgical prediction of ischemic mitral regurgitation recurrence using in vivo mitral valve leaflet strains. *Annals Biomed. Eng.* **49**, 3711–3723, DOI: <https://doi.org/10.1007/s10439-021-02772-5> (2021).
22. El-Tallawi, K. C. *et al.* Valve strain quantitation in normal mitral valves and mitral prolapse with variable degrees of regurgitation. *JACC: Cardiovasc. Imaging* **14**, 1099–1109, DOI: <https://doi.org/10.1016/j.jcmg.2021.01.006> (2021).
23. Biffi, B. *et al.* A workflow for patient-specific fluid–structure interaction analysis of the mitral valve: A proof of concept on a mitral regurgitation case. *Med. Eng. & Phys.* **74**, 153–161, DOI: <https://doi.org/10.1016/j.medengphy.2019.09.020> (2019).
24. Khalighi, A. H. *et al.* Development of a functionally equivalent model of the mitral valve chordae tendineae through topology optimization. *Annals Biomed. Eng.* **47**, 60–74, DOI: <https://doi.org/10.1007/s10439-018-02122-y> (2019).
25. Kong, F. *et al.* Finite element analysis of annuloplasty and papillary muscle relocation on a patient-specific mitral regurgitation model. *PLOS ONE* **13**, 1–15, DOI: <https://doi.org/10.1371/journal.pone.0198331> (2018).
26. Kong, F., Caballero, A., McKay, R. & Sun, W. Finite element analysis of mitralclip procedure on a patient-specific model with functional mitral regurgitation. *J. Biomech.* **104**, 109730, DOI: <https://doi.org/10.1016/j.jbiomech.2020.109730> (2020).
27. Sacks, M. *et al.* On the simulation of mitral valve function in health, disease, and treatment. *J Biomech Eng* **141**, 0708041–07080422, DOI: <https://doi.org/10.1115/1.4043552> (2019).
28. Villard, P.-F., Hammer, P. E., Perrin, D. P., del Nido, P. J. & Howe, R. D. Fast image-based mitral valve simulation from individualized geometry. *The Int. J. Med. Robotics Comput. Assist. Surg.* **14**, e1880, DOI: <https://doi.org/10.1002/rcs.1880> (2018). E1880 rcs.1880.

29. Wu, W. *et al.* The effects of leaflet material properties on the simulated function of regurgitant mitral valves. *J. Mech. Behav. Biomed. Mater.* **142**, 105858, DOI: <https://doi.org/10.1016/j.jmbbm.2023.105858> (2023).
30. Laville, C., Pradille, C. & Tillier, Y. Mechanical characterization and identification of material parameters of porcine aortic valve leaflets. *J. Mech. Behav. Biomed. Mater.* **112**, 104036, DOI: <https://doi.org/10.1016/j.jmbbm.2020.104036> (2020).
31. Rausch, M. K. & Kuhl, E. On the effect of prestrain and residual stress in thin biological membranes. *J. Mech. Phys. Solids* **61**, 1955–1969, DOI: <https://doi.org/10.1016/j.jmps.2013.04.005> (2013).
32. Aggarwal, A. *et al.* In-vivo heterogeneous functional and residual strains in human aortic valve leaflets. *J. Biomech.* **49**, 2481–2490, DOI: <https://doi.org/10.1016/j.jbiomech.2016.04.038> (2016). Cardiovascular Biomechanics in Health and Disease.
33. Wu, W. *et al.* A computational framework for atrioventricular valve modeling using open-source software. *J. Biomech. Eng.* **144**, 101012, DOI: <https://doi.org/10.1115/1.4054485> (2022).
34. Yushkevich, P. A. *et al.* Ic-p-174: Fast automatic segmentation of hippocampal subfields and medial temporal lobe subregions in 3 tesla and 7 tesla t2-weighted mri. *Alzheimer's & Dementia* **12**, P126–P127, DOI: <https://doi.org/10.1016/j.jalz.2016.06.205> (2016).
35. Aggarwal, A. *et al.* Strain estimation in aortic roots from 4d echocardiographic images using medial modeling and deformable registration. *Med. Image Analysis* **87**, 102804, DOI: <https://doi.org/10.1016/j.media.2023.102804> (2023).
36. Raissi, M., Perdikaris, P. & Karniadakis, G. Physics-informed neural networks: A deep learning framework for solving forward and inverse problems involving nonlinear partial differential equations. *J. Comput. Phys.* **378**, 686–707, DOI: <https://doi.org/10.1016/j.jcp.2018.10.045> (2019).
37. Lu, L., Meng, X., Mao, Z. & Karniadakis, G. E. DeepXDE: A deep learning library for solving differential equations. *SIAM Rev.* **63** (2021).
38. Karniadakis, G. E. *et al.* Physics-informed machine learning. *Nat. Rev. Phys.* **3**, 422–440 (2021).
39. Chen, Y., Lu, L., Karniadakis, G. E. & Negro, L. D. Physics-informed neural networks for inverse problems in nano-optics and metamaterials. *Opt. Express* **28**, 11618–11633, DOI: <https://doi.org/10.1364/OE.384875> (2020).
40. Yazdani, A., Lu, L., Raissi, M. & Karniadakis, G. E. Systems biology informed deep learning for inferring parameters and hidden dynamics. *PLoS computational biology* **16**, e1007575 (2020).
41. Lu, L. *et al.* Physics-informed neural networks with hard constraints for inverse design. *SIAM J. on Sci. Comput.* **43**, B1105–B1132 (2021).
42. Wu, W., Daneker, M., Jolley, M. A., Turner, K. T. & Lu, L. Effective data sampling strategies and boundary condition constraints of physics-informed neural networks for identifying material properties in solid mechanics. *Appl. Math. Mech.* **44**, 1039–1068, DOI: <https://doi.org/10.1007/s10483-023-2995-8> (2023).
43. Daneker, M., Zhang, Z., Karniadakis, G. E. & Lu, L. Systems biology: Identifiability analysis and parameter identification via systems-biology-informed neural networks. In *Computational Modeling of Signaling Networks*, 87–105 (Springer, 2023).

44. Wu, W., Daneker, M., Turner, K. T., Jolley, M. A. & Lu, L. Identifying heterogeneous micromechanical properties of biological tissues via physics-informed neural networks. *Small Methods* **n/a**, 2400620, DOI: <https://doi.org/10.1002/smt.202400620>.
45. Fan, B. *et al.* Deep learning for solving and estimating dynamic macro-finance models. *Comput. Econ.* 1–37 (2024).
46. Daneker, M. *et al.* Transfer learning on physics-informed neural networks for tracking the hemodynamics in the evolving false lumen of dissected aorta. *Nexus* **1** (2024).
47. Maas, S. A., Ellis, B. J., Ateshian, G. A. & Weiss, J. A. *Febio*: Finite elements for biomechanics. *J. Biomech. Eng.* **134**, DOI: <https://doi.org/10.1115/1.4005694> (2012).
48. Krishnamurthy, G. *et al.* Material properties of the ovine mitral valve anterior leaflet in vivo from inverse finite element analysis. *Am. J. Physiol. Circ. Physiol.* **295**, H1141–H1149, DOI: <https://doi.org/10.1152/ajpheart.00284.2008> (2008).
49. Herz, C. *et al.* Segmentation of tricuspid valve leaflets from transthoracic 3d echocardiograms of children with hypoplastic left heart syndrome using deep learning. *Front. Cardiovasc. Medicine* **8**, DOI: <https://doi.org/10.3389/fcvm.2021.735587> (2021).
50. Burk, K. M., Narayan, A. & Orr, J. A. Efficient sampling for polynomial chaos-based uncertainty quantification and sensitivity analysis using weighted approximate fekte points. *Int. J. for Numer. Methods Biomed. Eng.* **36**, e3395, DOI: <https://doi.org/10.1002/cnm.3395> (2020).
51. Bergquist, J. A. *et al.* Uncertainty quantification of the effect of cardiac position variability in the inverse problem of electrocardiographic imaging. *Physiol. Meas.* **44**, 105003, DOI: <https://doi.org/10.1088/1361-6579/acfc32> (2023).
52. Votta, E. *et al.* Toward patient-specific simulations of cardiac valves: State-of-the-art and future directions. *J. Biomech.* **46**, 217–228, DOI: <https://doi.org/10.1016/j.jbiomech.2012.10.026> (2013). Special Issue: Biofluid Mechanics.
53. Quarteroni, A., Manzoni, A. & Vergara, C. The cardiovascular system: Mathematical modelling, numerical algorithms and clinical applications. *Acta Numer.* **26**, 365–590, DOI: <https://doi.org/10.1017/S0962492917000046> (2017).
54. Bracamonte, J. H., Saunders, S. K., Wilson, J. S., Truong, U. T. & Soares, J. S. Patient-specific inverse modeling of in vivo cardiovascular mechanics with medical image-derived kinematics as input data: Concepts, methods, and applications. *Appl. Sci.* **12**, DOI: <https://doi.org/10.3390/app12083954> (2022).
55. Aly, A. H. *et al.* In vivo image-based 4d modeling of competent and regurgitant mitral valve dynamics. *Exp. Mech.* **61**, 159–169, DOI: <https://doi.org/10.1007/s11340-020-00656-8> (2021).
56. Simonian, N. T. *et al.* Patient-specific quantitative in-vivo assessment of human mitral valve leaflet strain before and after mitraclip repair. *Cardiovasc. Eng. Technol.* **14**, 677–693, DOI: <https://doi.org/10.1007/s13239-023-00680-4> (2023).
57. Laurence, D. W. *et al.* FEBio FINESSE: An open-source finite element simulation approach to estimate in vivo heart valve strains using shape enforcement. *arXiv e-prints* arXiv:2407.09629 (2024).
58. Aguilera, H. M. *et al.* Finite element analysis of mitral valve annuloplasty in barlow’s disease. *J. Biomech.* **142**, 111226, DOI: <https://doi.org/10.1016/j.jbiomech.2022.111226> (2022).

59. Mathur, M. *et al.* Texas trivalve 1.0 : a reverse-engineered, open model of the human tricuspid valve. *Eng. with Comput.* **38**, 3835–3848, DOI: <https://doi.org/10.1007/s00366-022-01659-w> (2022).
60. Stephens, E. H., de Jonge, N., McNeill, M. P., Durst, C. A. & Grande-Allen, K. J. Age-related changes in material behavior of porcine mitral and aortic valves and correlation to matrix composition. *Tissue Eng. Part A* **16**, 867–878, DOI: <https://doi.org/10.1089/ten.tea.2009.0288> (2010).
61. Pham, T., Sulejmani, F., Shin, E., Wang, D. & Sun, W. Quantification and comparison of the mechanical properties of four human cardiac valves. *Acta Biomater.* **54**, 345–355, DOI: <https://doi.org/10.1016/j.actbio.2017.03.026> (2017).
62. Rausch, M. K. *et al.* Mechanics of the mitral valve. *Biomech. Model. Mechanobiol.* **12**, 1053–1071, DOI: <https://doi.org/10.1007/s10237-012-0462-z> (2013).
63. Stevanella, M., Votta, E., Lemma, M., Antona, C. & Redaelli, A. Finite element modelling of the tricuspid valve: A preliminary study. *Med. Eng. Phys.* **32**, 1213–1223, DOI: <https://doi.org/10.1016/j.medengphys.2010.08.013> (2010).
64. Wang, Q. & Sun, W. Finite element modeling of mitral valve dynamic deformation using patient-specific multi-slices computed tomography scans. *Annals Biomed. Eng.* **41**, 142–153, DOI: <https://doi.org/10.1007/s10439-012-0620-6> (2013).
65. Lee, C.-H., Amini, R., Gorman, R. C., Gorman, J. H. & Sacks, M. S. An inverse modeling approach for stress estimation in mitral valve anterior leaflet valvuloplasty for in-vivo valvular biomaterial assessment. *J. Biomech.* **47**, 2055–2063, DOI: <https://doi.org/10.1016/j.jbiomech.2013.10.058> (2014). Functional Tissue Engineering.
66. Rausch, M. K. *et al.* In vivo dynamic strains of the ovine anterior mitral valve leaflet. *J. Biomech.* **44**, 1149–1157, DOI: <https://doi.org/10.1016/j.jbiomech.2011.01.020> (2011).
67. Fedorov, A. *et al.* 3d slicer as an image computing platform for the quantitative imaging network. *Magn. Reson. Imaging* **30**, 1323–1341, DOI: <https://doi.org/10.1016/j.mri.2012.05.001> (2012).
68. Lasso, A. *et al.* Slicerheart: An open-source computing platform for cardiac image analysis and modeling. *Front. Cardiovasc. Medicine* **9**, DOI: <https://doi.org/10.3389/fcvm.2022.886549> (2022).
69. Scanlan, A. B. *et al.* Comparison of 3d echocardiogram-derived 3d printed valve models to molded models for simulated repair of pediatric atrioventricular valves. *Pediatr. Cardiol.* **39**, 538–547, DOI: <https://doi.org/10.1007/s00246-017-1785-4> (2018).
70. Avants, B. B. *et al.* A reproducible evaluation of ants similarity metric performance in brain image registration. *NeuroImage* **54**, 2033–2044, DOI: <https://doi.org/10.1016/j.neuroimage.2010.09.025> (2011).
71. Avants, B., Epstein, C., Grossman, M. & Gee, J. Symmetric diffeomorphic image registration with cross-correlation: Evaluating automated labeling of elderly and neurodegenerative brain. *Med. Image Analysis* **12**, 26–41, DOI: <https://doi.org/10.1016/j.media.2007.06.004> (2008). Special Issue on The Third International Workshop on Biomedical Image Registration – WBIR 2006.
72. Joshi, S., Davis, B., Jomier, M. & Gerig, G. Unbiased diffeomorphic atlas construction for computational anatomy. *NeuroImage* **23**, S151–S160, DOI: <https://doi.org/10.1016/j.neuroimage.2004.07.068> (2004). Mathematics in Brain Imaging.
73. Rego, B. V., Pouch, A. M., Gorman, J. H., Gorman, R. C. & Sacks, M. S. Patient-specific quantification of normal and bicuspid aortic valve leaflet deformations from clinically derived images. *Annals Biomed. Eng.* **50**, 1–15, DOI: <https://doi.org/10.1007/s10439-021-02882-0> (2022).

74. Bonet, J. & Wood, R. D. *Nonlinear Continuum Mechanics for Finite Element Analysis* (Cambridge University Press, 2008), 2 edn.